Constraining the 410-km Discontinuity with Triplication Waveform

submitted to *Geophys. J. Int.*

Constraining the 410-km Discontinuity with Triplication Waveform

Jiaqi Li [1*], Min Chen [1,2], Jieyuan Ning [3], Tiezhao Bao [3], Ross Maguire [1,4] and Tong Zhou [5]

[1] *Department of Computational Mathematics, Science and Engineering, Michigan State University, East Lansing, Michigan* 48824*, USA. E-mail: lijiaqi9@msu.edu*

[2] *Department of Earth and Environmental Sciences, Michigan State University, East Lansing, Michigan* 48824*, USA.*

[3] *School of Earth and Space Sciences, Peking University, Beijing* 100871*, China.*

[4] *Department of Earth and Planetary Sciences, University of New Mexico, Albuquerque, NM,* 87131*, USA.*

[5] *Earth, Planetary and Space Sciences, University of California Los Angeles, CA,* 90095*, USA.*

SUMMARY

The detailed structures near the 410-km discontinuity provide key constraints of the dynamic interactions between the upper mantle and the lower mantle through the mantle transition zone via mass and heat exchange. The 410-km discontinuity topography inside the slab could be used to infer the existence of the metastable olivine wedge, further investigate the possible mechanism for deepfocus earthquakes. Multipathing, i.e., triplicated, body waves which bottom near the 410-km discontinuity carry rich information of this discontinuity, such as interface depth and wave speed jump across it. In this study, we investigated the frequency dependent resolution of triplicated waveforms sampling the 410-km discontinuity and explore the tradeoffs between wave speed and discontinuity depth. Additionally, we proposed the array-normalization technique. Finally, with the non-gradient-based inversion package we have developed, we derived a 1-D depth profile of the wave speed below the Tatar Strait of Russia. The inverted model shows an uplift interface at 400±5 km, with a significant wave speed jump of $\sim$ 7%-8%, which is 2%-3% larger than that of the IASP91 model. We proposed this interface to be an overlapping of the uplifted 410-km discontinuity and the slab upper interface. Our preferred slab upper interface, from the simultaneous inversion of the interface depth and the wave speed using high frequency waveforms ($\sim$ 0.5 Hz), is $\sim$ 50-70 km shallower than the Slab2.0 model and the +2-3% wave speed contours of the regional tomography model.

Key words: 410-km discontinuity; triplication; non-gradient-based inversion; subducting slab

1 INTRODUCTION

The 410-km discontinuity marks the top of the mantle transition zone (MTZ). This interface represents the mineralogical phase change of olivine to wadsleyite at around 410 km, demonstrated by laboratory experiments (Ringwood 1975). The detailed structures near the 410-km discontinuity provide key constraints of the dynamic interactions between the upper mantle and the lower mantle through the MTZ via mass and heat exchange.

One of the essential interactions involves cold slabs penetrating and elevating the 410-km discontinuity and carrying volatiles into the transition zone (Kawakatsu & Watada 2007). At this pressure-temperature induced phase transition interface, the pressure (depth) and the temperature is one-to-one correlated. Therefore, the 410-km discontinuity depth provides an in situ thermometer near the top of the mantle transition zone. The 410-km discontinuity thickness (sharpness) is sensitive to the water content (Helffrich & Wood 1996; Van der Meijde et al. 2003), which could provide insight into the deep Earth's volatile budget (Thompson, 1992).

⋆ E-mail: lijiaqi9@msu.edu

Although deep-focus earthquakes and cold temperatures in the subducting slab are associated, the mechanism for deep-focus earthquakes is still unclear. Interaction between the 410-km discontinuity and the subducting slab could reveal this critical question. Specifically, the 410-km discontinuity topography inside the subducting slab could be used to infer the existence of a meta-stable olivine wedge, a candidate to account for deep-focus earthquakes (Green Ii & Burnley 1989; Kirby et al. 1991).

To detect and further constrain the discontinuity, secondary seismic phases generated at the interface could be good candidates. The related methods can generally be classified into two categories: one is to use the reflected waves off the interfaces (e.g., Flanagan & Shearer (1998, 1999); Gu & Dziewonski (2002); Schmerr & Garnero (2007); Houser et al. (2008); Lawrence & Shearer (2008); Ritsema et al. (2009b); Wang et al. (2017); Li et al. (2019); Tian et al. (2020); Wei et al. (2020)); and the other is to use the converted wave upon transmissions at the discontinuities (e.g., Vinnik (1977); Collier & Helffrich (1997); Thirot et al. (1998); Chevrot et al. (1999); Niu et al. (2005); Ritsema et al. (2009a)). Although these secondary phases could provide direct constraints on the discontinuities, stacking over hundreds of traces is usually necessary to enhance the visibility of these minor phases.

An alternative approach is to use the regional (10^o - 30^o) multipathing seismic body waves which bottom near the interface. Unlike the phase conversions and reflections which are too weak to observe on individual seismogram, these multipathing waves (triplications) are clearly recorded at a single station. Moreover, distinct triplication branches with different move-out slopes can be observed in record sections of dense seismic arrays.

Since 1967, travel times of triplicated body-wave phases have been used to constrain the 1-D upper mantle structure (Johnson 1967). Later on, waveform matching, between observed and synthetic seismograms has been used to find the best fitting 1-D wave speed profile (e.g., Grand & Helmberger (1984); Tajima & Grand (1995); Brudzinski & Chen (2000); Wang et al. (2009)). However, due to the complexity of the waveforms, most of these studies rely on a trial-and-error approach.

Some efforts towards the automatic inversion have been made by applying the conjugate gradient method (Gao et al. 2006). However, for this gradient-based method, finding an appropriate initial model to avoid falling into the local minima is challenging, especially for the complex triplication data. Moreover, the inverted model's quantitative error estimation is hard to derive (Shearer 2000), and possible tradeoffs between model parameters need systematic considerations.

With the rapid development of full-waveform inversion (FWI), triplicated waveforms are also recently incorporated into the 3-D FWI framework (Tao et al. 2018). Nevertheless, the shortest period for regional FWI is $\sim$ 8s due to the vast computational cost for a higher frequency, which limits the resolution. Also, the currently available data may still not be adequate to constrain 3-D models well. For both reasons, 1-D simulation and inversion, using high frequency data (up to $\sim$ 1 Hz) and few parameters, is still a useful approach to reveal the structure in certain regions, especially near the turning points of seismic waves.

In this paper, we first analyze broadband triplicated waveforms for several typical model situations to reveal their sensitivity to such features and possible tradeoffs between model parameters. Then we introduce a 1-D non-gradient-based inversion scheme, with which we invert the 1-D structure below the Tatar Strait. Finally, we discuss possible 2-D influence on the 1-D triplication inversion results.

2 METHOD

2.1 Multipathing triplicated body waves

Triplications originate when seismic body waves encounter regions where wave speed increases sharply with depth (e.g., the Moho, the 410-km discontinuity, and the 660-km discontinuity). Near such discontinuities or steep gradients, body waves (both P and S waves) will propagate in different paths. Fig. 1a shows an example of the raypath geometry and corresponding synthetic seismograms of P-wave triplications caused by the 410-km discontinuity. To clearly show the triplicated phases, in this section we use the WKBJ code of Chapman (1978), which enables us to separately calculate each of the three branches. The synthetics are computed using the seismic reference model IASP91 (Kennett & Engdahl 1991), assuming an earthquake source at 114 km depth. The three branches consist of the direct branch (AB), the reflected branch (BC), and the refracted branch (CD), which are illustrated in Fig. 1b, 1c, and 1d, respectively. We use the source-receiver geometry shown in Fig. 1 for synthetic tests throughout this study, although subsequent modeling uses more realistic attenuation (t^* of 1 s) and a Gaussian source time function, instead of the stick diagram here. As shown in Fig. 1, these triplicated phases provide dense sampling of the 410-km discontinuity. Since the raypaths of the different triplication branches deviate only slightly from each other in the shallow mantle, the relative travel times and amplitudes of triplications can be attributed primarily to the structure near the transition zone.

2.2 Frequency dependent resolution for discontinuity sharpness

The depth interval over which the olivine to wadsleyite transition occurs is sensitive to the water content (Helffrich & Wood 1996). Therefore constraining the sharpness of the 410-km discontinuity is critical for understanding the Earth's deep water cycle. Mineralogical and thermodynamic modeling suggests that the width of the olivine-wadsleyite phase transition is between 7 km and 19 km (Akaogi et al. 1989; Gaherty et al. 1999; Katsura et al. 2004). However, many seismological results have found a narrower range of 10 km or less (Benz & Vidale 1993; Vidale et al. 1995; Neele 1996; Tibi & Wiens 2005). On the other hand, there is also seismological evidence that the 410-km discontinuity is much broader (20-35 km) in regions with previous subduction, suggesting a hydrated MTZ (Van der Meijde et al. 2003). Therefore, quantitative estimation of the resolution and the uncertainty is indispensable to figure out this discrepancy and further understand the deep water cycle of the Earth.

For body wave triplication data, we want to explore its sensitivity to the discontinuity's sharpness through forward modeling. We set the 410-km discontinuity location in the IASP91 model as the midpoint and vary the thickness between 20 km and 40 km (Fig. 2a). For this modeling here and all the others in subsequent parts, we use the QSEIS program (Wang 1999) to calculate the full wave field, instead of specified phases by the WKBJ program in Fig. 1.

Travel time curves show that the increasing of the discontinuity thickness has the strongest impact on the BC branch. Specifically, the thickened discontinuity will considerably "shrink" the reflected wave branch BC, although it has little effect on the arrivals of the direct wave branch AB and the transmitted wave branch CD (Fig. 2b).

However, the corresponding waveforms seem to show different conclusions from the travel time curves. Specifically, no noticeable difference of the BC branch can be seen even the thickness of the discontinuity increases to 40 km (Fig. 2c). This discrepancy is because the travel time curve is calculated based on the ray theory (Crotwell et al. 1999). However, this waveform modeling period is about 3s, where wavefront healing occurs due to the finite frequency effect.

To further study this frequency dependent feature, we performed forward modeling for the model with a discontinuity thickness of 40 km with different duration for the source time function of 3 s, 2 s, and 1 s, respectively (Fig. 2c, 2d, 2e). Results show that as the frequency increases, the waveform differences between this gradual model and the sharp IASP91 model become more apparent (especially for the pre-critical reflections at a smaller epicentral distance). Moreover, when the waveform period is greater than 3 s, it is impossible to distinguish the discontinuity between a sharp interface and a gradual one with 40 km thickness, even without adding noise. A similar frequency dependent feature has also been observed in previous triplication studies (Melbourne & Helmberger 1998; Zhang et al. 2019).

To provide more constraints on the discontinuity's sharpness, we could filter the broadband record into short-period data, but at the cost of losing other useful information. An alternative way is to choose smaller events with a shorter source time function. However, there always exists a contradiction between the smaller events and the lower SNR. Nevertheless, combining triplication data with converted or underside reflected phases could better constrain the discontinuity's sharpness.

2.3 No tradeoff between discontinuity depth and wave speed in the MTZ

Temperature variations could cause the phase transition interface's undulation, as shown by the phase transition kinetics experiments (Ringwood 1968). For the 410-km discontinuity, this equilibrium phase change interface from olivine to wadsleyite can be elevated in the presence of cold temperatures, such as near subducting slabs (e.g., Flanagan & Shearer (1998)) due to the positive Clapeyron slope (e.g., Bina & Helffrich (1994); Katsura et al. (2010); King et al. (2015)).

Fast P-wave speed in the MTZ has been observed in a particular region beneath the Tonga backarc (Brudzinski & Chen 2000). In the western Pacific subduction zone, tomography results (Huang & Zhao 2006; Chen & Pei 2010) indicate a 'flat slab' in the MTZ, which also increases the wave speed in the mantle transition zone.

We first test the triplication's sensitivity to the higher wave speed in the MTZ. Here we calculated the travel time curves when the wave speed below the 410-km discontinuity is increased by 0.1 km/s (Fig. 3b) relative to the IASP91 model, using the Taup toolkit (Crotwell et al. 1999). Travel time curves show that the MTZ's wave speed significantly impacts the CD branch's travel time (Fig. 3d). In other words, the increase of the wave speed below the discontinuity will make the transmitted waves (CD) travel faster, which will cause the crossover point (O) of the AB branch and the CD branch to appear at a smaller epicentral distance.

However, when the 410-km discontinuity has a 30-km uplift (Fig. 3a), the CD branch also arrives earlier (Fig. 3c). Similarly, the crossover point (O) occurs at a smaller distance. This is because, in this situation, this elevated interface is equivalent to a high wave speed anomaly between 380 km and 410 km.

Nevertheless, careful waveform analysis could distinguish between these two situations. Specifically, in the case of a more considerable wave speed jump, the amplitude near cusp B remains unchanged (shaded gray area in Fig. 3f). On the other hand, with an uplifted 410-km discontinuity, the amplitude near cusp B is smaller (shaded gray area in Fig. 3e).

Therefore, even if the travel time differences between the OB and OD branches are almost identical for these two situations (Fig. 3c and 3d), with waveform information recorded by seismic array, we can make unambiguous distinction between them.

2.4 The tradeoff between discontinuity depth and low wave speed above the 410-km discontinuity

Some research indicates a low wave speed zone above the 410-km discontinuity in the north-eastern region of Asia (Revenaugh & Sipkin 1994; Tajima & Grand 1995; Wang & Chen 2009). Such a low wave speed zone atop the 410-km discontinuity has also been observed sporadically in regions of the western United States (Song et al. 2004; Schmandt et al. 2011) and Pacific Ocean (Wei & Shearer 2017). Its existence, indicative of partial melting, will provide evidence for the water content in the mantle transition zone (Bercovici & Karato 2003).

We calculated both the travel time curves and waveforms when the wave speed gradient was decreased by 0.1 km/s within 50 km above the 410-km discontinuity (Fig. 4a). The low wave speed zone above the discontinuity mainly affects the extension of the OB branch (Fig. 4b). Specifically, in this case, the direct waves (OB branch) terminates at a larger epicentral distance, thereby increasing the OB branch's amplitude (Fig. 4c). Meanwhile, the travel time will not be significantly affected because the low wave speed area only exists within 50 km right above the 410-km discontinuity.

Forward modeling shows that the most sensitive change of triplication waveforms to the low wave speed layer is the OB branch's extension. However, other model parameters could also cause such equivalent behavior near cusp B. We know that an uplifted interface will shorten the OB branch's extension from synthetic tests (Fig. 3e). In turn, a depressed interface will lengthen it.

Here we show a comparison between the model with a depressed interface but with a normal wave speed gradient (the blue line in Fig. 4a), with the model without depth change but with a low wave speed layer above the interface (the red line in Fig. 4a). The travel time curves (Fig. 4b) show that both of these two models will extend the OB branch to farther distance, and the model with a low wave speed layer above the interface has longer extension. However, within the range where the OB branch is large enough to observe, the waveforms of these two models are quite similar (shaded gray area in Fig. 4c and Fig. 4d). We should note that, in this case, the travel time curves show some discrepancies with the amplitude of the waveforms. This inconsistency comes from the difference between the ray theory and the finite frequency effect. The waveform comparison, which takes the finite frequency effect into account, is more reliable and closer to the real situation.

Therefore, triplication data alone cannot well-constrain a low wave speed zone due to the tradeoff between the interface's depth and the wave speed gradient above it. Nevertheless, for a given frequency band, we could estimate the depth uncertainty due to this tradeoff. One possible approach is to compare waveforms between possible models to find the acceptable minimum and maximum depth limits for the interface. These depth limits can be quickly found using the automatic inversion program, which we will introduce in the next section.

2.5 Non-gradient-based inversion

To obtain quantitative error bounds and avoid the risk of falling into the local minima faced by the gradient-based inversion method, we adopt the niche genetic algorithm (Koper et al. 1999; Li et al. 2012) into the inversion framework of triplicated waveforms. Niche genetic algorithm (NGA) is a non-gradient-based inversion scheme that searches the model space through massive forward modeling. NGA is independent of the initial model. Only the search range of the model space is given as a priori. Moreover, because NGA involves numerous samplings in the model space, it can finally output a series of acceptable model sets. The mean and variance of these acceptable models can help estimate the uncertainty of the final model.

We designed a P-wave synthetic test to verify the NGA inversion framework. In this test, we set the IASP91 model as the "ground truth", and let its corresponding synthetic displacement waveforms be inverted. In the inversion model setup, considering the ray paths' penetration depths, we only invert the structure from 210 km to 560 km depth. Within this depth range, totally we set nine parameters to invert. Specifically, three parameters are on the '410-km' discontinuity to capture the sharp gradient: two of them are immediately on the discontinuity to represent the wave speed jump, another one is its depth variation. In addition, three parameters are set with an interval of $\sim$ 40 km, above and below the interface, respectively. We should note that for these six anchor points which reflect more gradual wave speed change away from the discontinuity, we only invert the wave speed at these points. Between two adjacent points, the wave speed is linearly interpolated. Beyond this depth range, the wave speed is fixed to the value in the IASP91 model. The P wave speed at each anchor point is allowed to vary between plus and minus 0.3 km/s, and the position of the discontinuity varies within plus or minus 20 km, based on the IASP91 model (Fig. 5a). The

P wave speed is the only unknown parameter for each anchor point, and the Poisson's ratio and density are the same as those in the IASP91 model. The effect of attenuation for P wave is considered by applying a constant t* values of 1s.

As for the misfit window, we choose a continuous one from 32 s to 52 s (reduced time) which contains the entire triplicated P wave train, for this ideal case without noise. Prior to the calculation of the misfit, we first cross-correlate the theoretical and observed waveform for the ith station to obtain the time difference Δt_i. After shifting the synthetic trace by Δt_i, we calculate the L2 norm of the differences between the observed and aligned synthetic waveform in the time domain as the misfit function χ_{L2}:

$$\chi_{L2} = \sum_{i=1}^{N} \int_{t_1}^{t_2} |\mathbf{d}(\mathbf{x}_i, t) - \mathbf{u}(\mathbf{x}_i, t + \Delta t_i)|^2 dt, \tag{1}$$

Where, $\mathbf{d}(\mathbf{x}_i, t)$ is the displacement data recorded by the ith station, $\mathbf{u}(\mathbf{x}_i, t + \Delta t_i)$ is the synthetic data for the ith station after a time shift of Δt_i. t_1 and t_1 are the start and end time for the misfit window, respectively. N is the total number of stations used in the inversion.

This method converges very quickly. After the first 20 generations (100 simulations per generation), the residuals significantly reduce. And after 80 generations, the residuals are stable (Fig. 5c). From the 100 models in the last generation, we further define the acceptable model limits by a 10% increase in the misfit than the best model or by visually comparing the data and synthetics when the misfit does not readily detect the mismatch.

Finally, we have got three typical acceptable model groups (Fig. 5a). We take two of them as an example. The first model group (in red color) is very close to the input IASP91 model, and another model group (in blue color) shows a 10-km uplift of the discontinuity and a low wave speed zone above the interface. We further use the averaged value of these two groups of models to calculate their corresponding displacement waveforms, respectively. Waveforms between these two groups are almost identical, and both of them are also quite similar to the IASP91 model's waveforms (Fig. 5b).

This synthetic test shows that our triplication inversion scheme can effectively obtain a model with good waveform fits. Furthermore, the non-uniqueness of the inverted model also shows that, given this frequency band and misfit tolerance, the tradeoff from the wave speed above the discontinuity will lead a $\sim$ 10 km uncertainty to the depth estimation.

3 APPLICATION TO THE KURIL SUBDUCTION ZONE

We focus on an intermediate depth (114 km) event occurred in the Kuril subduction zone on October 10, 2009 with Mw $\sim$ 5.9 (Fig. 6a), to study the depth variation of the 410-km discontinuity due to the cooling effect from the cold slab. This study's triplication waveforms are from a subset of the broadband NECESSArray (NorthEast China Extended Seismic Array) and CEArray (Zheng et al. 2010) in northeast China. We choose the P-wave data to achieve a better resolution, because P wave is typically observed at higher frequency than S wave due to its smaller attenuation. Therefore, even though the wave speed of the P wave is faster than that of the S wave, P wave still has a smaller Fresnel zone. After removing the instrument response, we have applied a first-order, zero-phase shift Butterworth filter with frequency band 0.05-1 Hz to the data. We choose this relatively broad frequency band to avoid distortion of the data. Because the azimuth range of this selected sublinear array is relatively narrow (2^o), one model should explain all the waveforms in the record section.

Given the fact that with this triplication data alone we cannot exclusively judge the presence of a low wave speed zone above the 410-km discontinuity, therefore we fix the gradient above the interface a priori to be the same value as the IASP91 model. As such, we can focus more on the first order location of the discontinuity. But we should know that at this frequency band, the tradeoff from the low wave speed gradient above will introduce a depth uncertainty $\sim$ 10 km (Fig. 5a).

In addition, according to the synthetic tests, given the duration of the source time function $\sim$ 2 s, we cannot discern a model with a sharp jump across the 410-km discontinuity from the model with a gradual interface with a 20-km width. Therefore, in the inversion, we set the discontinuity as a sharp interface. Nevertheless, the inverted interface's depth should coincide with the center of the actual (perhaps wider) interface.

The waveform fitting generally shows good agreement for both the relative timing and amplitudes in each trace and the amplitude variations between stations (Fig. 6b). The only mismatch exists for station 'NE9E' with epicentral distance $\sim 13^o$, where the reflected phase is much weaker in the data (green circle in Fig. 6b). We have tested various possible 1-D models with proper fitting for the travel time, but none could produce such a weak amplitude. Specifically, take one candidate model with a broaden 410-km discontinuity as an example, although this broaden interface can lower the amplitude of the BC branch (pre-critical reflections) near cusp C, it won't change the amplitude of it near the crossover point O (Fig. 2e), which is what we see in this real data case. Therefore, we speculate that this unusual weak reflected phase might due to the localized, small-scale undulation of the 410-km discontinuity.

The inversion results show that the 410-km discontinuity for the best fitting model is located at 400 km depth (Fig. 6d). Based on all the acceptable models, the depth uncertainty is estimated to be 5 km. Here, this 5-km uncertainty is from the data itself. If we consider the tradeoff between model parameters, another 10-km uncertainty should be taken into account.

4 DISCUSSION

4.1 Array normalization

In this paper, we normalize all traces relative to one particular reference station. However, in most of the previous triplication studies, people prefer to normalize the waveforms by each trace. Normalization is needed because of the uncertainties in the source magnitude, fault plane solution, attenuation, and station site effects, which make the absolute amplitudes more difficult to constrain. However, when using the normalized amplitude of each trace, information about the waveform changes between stations is lost.

In this paper, we propose to use array normalization rather than trace normalization. In a record section, array normalization means that we normalize all traces relative to one particular reference station. Because all the records are from the same earthquake, the source magnitude's uncertainty will not affect the results after array normalization. Besides, within the narrow azimuthal range for the particular record section, the effect of uncertainty in the fault plane solution is also slight. When we invert for one discontinuity, the range of epicenter distance is only about within ten degrees. Therefore, we expect the attenuation near the discontinuity within this relatively smaller range should not change dramatically. Nevertheless, suppose we have observed stations with unusual amplitudes either due to attenuation or site effects, we could use trace normalization for these certain stations or reduce the weighting for them.

We compare the trace normalization and array normalization in one forward modeling case to illustrate the array normalization necessity. In Fig. 7c and Fig. 7d, the black model shown is the IASP91 model, and the red model is a designed model with a -0.4 km/s low wave speed layer only in the shallow part ($\sim$ 150 km). As shown in Fig. 7a, the array-normalized amplitudes of the waveforms demonstrate that the shallow part's different structures will cause an overall time delay (of $\sim$ 3 s) and affect the amplitude of the direct wave (AO). In comparison, the amplitudes of the later phases (CO) remain basically unchanged. However, for trace normalization, because the amplitude for direct wave (AO) is always the largest within the epicentral distance range before 15^o, the direct wave's amplitude is always unity after normalization (Fig. 7b). Therefore, the amplitude of the later phases (CO), whose amplitude is originally unchanged, seems to have a smaller amplitude after the trace normalization. We should note that the later phases correspond to the reflected wave at the 410-km discontinuity and the transmitted wave below it. In this way, the deeper structure will be incorrectly adjusted, whether through trial-and-error or automatic approach (Fig. 7d).

As such, trace normalization will lose the waveform information between stations and will lead to misunderstanding of the corresponding structure for the waveform's mismatch, which further affects the inversion result. Therefore, we recommend using an array-normalization approach.

4.2 Alignment prior to the inversion

For a given triplication trace, it contains two parts of information. One is the absolute time of the first arrival, and the other is the relative time and amplitudes between the triplicated phases. The absolute arrival time reflects the overall impact of the structure on the entire path. On the other hand, the relative time and amplitudes among the triplicated phases mainly reflects the structure near the turning points where the ray paths are separated.

If there is sufficient data coverage and precise earthquake source parameters, we can constrain both the absolute time and the relative information simultaneously. However, for teleseismic body waves, the shallow portion of the ray paths are usually sparse and parallel to each other, which hinders resolution of the shallower structure. Additionally, the earthquake's location and origin time are difficult to precisely determine, and other uncertainties exist, such as clock error or site effect. All of these factors introduce uncertainties in absolute time. Therefore, if the absolute time is considered, not only is it difficult to accurately resolve the full structure, but the timing error and unconstrained shallow structure will further contaminate the deeper structure (Li et al. 2016).

To minimize the contamination from the shallow parts, some researchers fix the shallower part according to other's model, and only invert the deeper structure (Ye et al. 2011). However, when the fixed shallow structure is inaccurate, this contamination still exists. The alternative way is to align the synthetic waveforms with the observed waveforms to get rid of the absolute time, and mainly analyze the relative time and amplitudes (Grand & Helmberger 1984; LeFevre & Helmberger 1989; Brudzinski & Chen 2003; Wang & Niu 2010; Chu et al. 2012; Zhang et al. 2012). In this way, the alignment operation will cancel out some baseline shifts (e.g., timing error) and highlight the deeper structures that are more sensitive to the relative time and amplitudes among the triplicated phases.

Applying this alignment correctly and effectively requires careful considerations. This is because there are more than one phase in the triplication wave train. One practical way is to align the data and synthetics according to their first arrivals. However, the first arrivals' penetration depths vary significantly with respect to epicentral distance, especially for triplication. Specifically, the first arrival could either be the direct wave (AB) above the discontinuity or the refracted wave (CD) below it. In either case, when a particular phase is selected as a reference phase for alignment, this specific phase will have much less misfit since it has already been aligned, compared with the un-aligned later arriving phase.

In other words, the alignment operation introduces an assumption that there are fewer anomalies along the ray path for this particular reference phase. However, in the real situation, this assumption cannot be guaranteed. This issue is exceptionally severe in the gradient-based inversion scheme. Specifically, it will modify the structure along the ray paths of the un-aligned phases that contribute most to the misfit.

Nevertheless, this is not an issue in the non-gradient-based inversion scheme because the model updating is no longer dependent on the 'biased' gradient calculated from the un-aligned phases. Instead, no matter the new model will change the later phase or the pre-aligned first phase, as long as it could enhance the waveform similarity, it is a candidate. We should also note that we redo the alignment in each iteration with the newly derived model, and the misfit is also calculated based on this new round of alignment.

Therefore, in the non-gradient-based inversion framework, alignment operation could effectively measure the differential travel time and amplitudes between triplicated phases without introducing any assumptions. Furthermore, because which phase is the reference phase is no longer an issue, we could use cross-correlation to align the entire triplication wave train, which is very practical in the inversion.

Here we designed synthetic tests to validate this alignment-based inversion scheme. To represent more general situations, we consider lateral heterogeneities in the upper 50 km of the subsurface. Specifically, we set a 50-km thick P-wave low wave speed anomaly zone (-0.3 km/s than the IASP91 value) in a particular area where the epicenter distance is less than 13.5^o (Fig. 8a) to qualitatively represent the low wave speed anomaly observed in regional tomography results (Fukao et al. 2001; Tao et al. 2018). From the forward waveforms calculated by a 2-D finite-difference method (Li et al. 2014), we can see that the arrivals of the nearer stations ($< 13.5^o$) have a significant overall time delay compared with farther stations ($> 13.5^o$). The offsets of the bold red lines and bold green lines in Fig. 8b also show this travel time delay.

In the waveform comparison results (Fig. 8b), the green waveforms are the 1-D synthetics (red waveforms) after cross-correlation alignment. Except for the slightly small amplitudes, they agree with the ground truth waveforms (black). Furthermore, the derived models from the best model group also converge to the ground truth model near the 410-km discontinuity (Fig. 8c).

1-D triplication inversion with the alignment strategy can minimize this 2-D inaccurate shallow structure's influence, mainly for two reasons: one is due to the constraints from the amplitude variations between stations. Although the 2-D model is very different in the shallow part from the 1-D model, in the deeper part it is the same as the IASP91 model. Therefore, only when the deeper parts are consistent, can the amplitudes between stations be fitted. Specifically, the station at 13.6^o has a more significant time advance than the station at 13.3^o. However, the waveform amplitude has no noticeable change, which implies that this advance in travel time is from the shallower area. In other words, if this earlier arrival is due to the deeper part, it should come from a high wave speed layer between the rays' penetration depths for these two stations (190 km to 210 km). Therefore, this localized anomaly will significantly increase the amplitude of the waveform at 13.6^o. However, we have not observed any corresponding amplitude increase in the waveforms.

The other constraint comes from the relative time between the direct wave, the reflected wave, and the transmitted wave in each trace. For example, if the anomaly originates from the shallow part, the time shifts for all the triplicated phases in each trace are quite similar. On the other hand, if the anomaly originates from the deep part, the impact on the three phases will be different. Specifically, if the anomaly locates in the range of 250 km to 410 km, it will have the most significant impact on the direct wave; if the anomaly is below 410 km, it will mostly impact the transmitted wave. Either way, the relative timing between the phases will be changed, and we cannot simultaneously fit all these triplicated phases in each trace.

This synthetic test shows that the 1-D non-gradient-based triplication inversion method can accurately and quickly obtain the results. Although it is a 1-D inversion, it is suitable for some situations with unknown lateral heterogeneity in the shallow part with the alignment strategy.

4.3 Uplifted 410-km discontinuity

The turning points, the most sensitive regions of the triplicated ray paths, are below the Tatar Strait of Russia. Our derived interface at 400 ± 5 km is consistent with the overall 0-10 km uplift of the 410-km discontinuity in this region observed with ScS reverberations (Wang et al. 2017). Furthermore, our result is of higher resolution due to the smaller Fresnel zone for P wave at higher frequency ($\sim$ 0.5 Hz).

Wang et al. (2014) and Tao et al. (2017), through waveform modeling, have shown that some 2-D and 3-D slab structures near the turning points can influence triplicated waveforms. To avoid this interference, we specifically choose the event whose ray paths are roughly parallel to the slab's depth contour. As such, in this particular direction, the slab seems to be flat near the turning points (Fig. 6c) and it can still satisfy the 1-D inversion assumption. Therefore, the inverted discontinuity depth of 400$\pm$5 km, derived from 1-D inversion, is reliable.

However, as for the implication of this uplifted interface, there is more than one explanation. Specifically, this uplifted interface located at 400$\pm$5 km can be the uplifted 410-km discontinuity. If this is the case, it is related to the cooling effect from the slab located $\sim$ 50-70 km below the discontinuity (Fig. 6c). The reported Clapeyron slopes for this olivine-wadsleyite phase transition interface vary from 2.9 MPa/K (Bina & Helffrich 1994) to 4.0 MPa/K (Katsura et al. 2004). Assuming a Clapeyron slope of 4.0 MPa/K from X-ray diffraction (Katsura et al. 2004), this 10$\pm$5 km uplift corresponds to a 50-150 K temperature decrease than the surrounding mantle.

On the other hand, although the Slab2.0 model (Hayes et al. 2018) and the +2%-3% wave speed contours of the regional tomography results (Tao et al. 2018) indicate a deeper slab at $\sim$ 450-470 km, it is challenging to define the precise location of the slab. First, the speculated slab upper surface from Slab2.0 model is based on an assumed thickness of the subducting oceanic lithosphere. Second, for the current tomography results, the structure near the discontinuity is less constrained than the region farther away from it, because the discontinuity depth is fixed in the tomography method (Tao et al. 2018).

Therefore, this derived interface can also be an overlapping of the 410-km discontinuity and the upper surface of the subducting slab. We should note that given the period band of $\sim$ 2 s we use, it could be considered as an overlapping when the distance between the slab upper interface and the 410-km discontinuity is within $\sim$ 20 km.

Nevertheless, because we simultaneously invert the wave speed and the interface depth at high frequency ($\sim$ 0.5 Hz), the averaged model in this region (epicentral distance of 6^o-12^o) with an interface at 400$\pm$5 km should be correct.

4.4 High wave speed jump across the discontinuity

As for the inverted wave speed, we should note that there could be a baseline shift in our inverted models because we cannot constrain the absolute wave speed value due to the cross-correlation alignment we used. Therefore, instead of the absolute wave speed, we pay more attention to the wave speed jump across the discontinuity, which is much better constrained.

From the synthetic test in Fig. 5a, we notice that the inverted models might have some small scale wave speed deviations from the ground truth model below the interface. However, these deviations vanish when it is farther away from the interface. These artifacts are probably due to the inversion parameterization and the frequency dependent resolution issue. Therefore, it is not appropriate to directly use the points immediately above and below the interface to calculate the wave speed jump. Instead, we choose the points 20 km above and below the inverted interface to measure the wave speed jump for both the inverted model sets and the IASP91 model. In this way, the wave speed jump across the discontinuity is 7.4%-8.5%.

This method of measurement over a distance of 40 km can minimize some artifacts. However, the wave speed jump of 7.4%-8.5% is still significantly larger than the value of 5.2% in the IASP91 model. This extra $\sim$ 2%-3% wave speed jump, could be due to two reasons: 1) the failure of the 1-D assumption in the source region; 2) the subducting slab near the turning points.

First, a cold slab in the source area might partly account for this extra $\sim$ 2%-3% wave speed jump. This is because near the source site, the high wave speed slab is roughly parallel to the ray paths. Although using relative time and amplitudes of the triplicated phases could eliminate the effect of lateral heterogeneities at shallow depth, this accumulated effect of the source-site anomalies along the ray paths cannot be neglected (Li et al. 2016). Therefore, this extra $\sim$ 2%-3% wave speed jump may be partly overestimated due to the failure of the 1-D assumption near the source site.

This extra $\sim$ 2%-3% wave speed jump could also come from the subducting slab just below the interface. As mentioned before, the upper surface of the subducting slab could coincide with the uplifted 410-km discontinuity. As such, a subducting slab, with colder temperature and larger portion of the olivine could account for this extra wave speed jump (Xu et al. 2008).

Based on these, we propose that our derived interface at 400$\pm$5 km, with an significant wave speed jump, indicates the averaged location of the 410-km discontinuity and the slab upper surface. In this way, the upper surface of the subducting slab we preferred is located $\sim$ 50-70 km shallower than the Slab2.0 model and the +2-3% wave speed contours of the regional tomography results (Tao et al. 2018).

Consistently, we found that in the regional tomography results (Tao et al. 2018), the +1% wave speed contour seems to be distorted near epicentral distance $\sim 9^o$ in Fig. 6c. The existence of this localized high wave speed feature to some extent confirms our inverted larger wave speed jump.

However, the value of this wave speed contour, in the regional tomography results (Tao et al. 2018), might be underestimated. Specifically, if this localized high wave speed anomaly within 2^o is expected to have the equivalent effect on the waveforms compared with our derived 1-D averaged model over 6^o, much higher wave speed is required. This underestimation might due to the inadequate ray paths in this region, where is close to their inversion boundary (Tao et al. 2018).

Nevertheless, if this derived extra $\sim$ 2%-3% wave speed jump is not totally overestimated, it should reflect the subducting slab just below the discontinuity. To further constrain the precise wave speed jump, 2-D or 3-D corrections are needed which take the source-site influence into account. In addition, in order to untangle the 410-km discontinuity and the upper surface of the subducting slab, more events and stations are needed to obtain a 2-D mapping of the discontinuities here.

5 CONCLUSIONS

Triplicated body waves have rich information and can effectively sample the structure near the transition zone. Although 1-D triplication inversion is a useful and efficient approach, its resolution limit and tradeoffs between model parameters should be carefully considered.

We have investigated the frequency dependent resolution for triplication, and proposed the necessity of using array-normalized data through examples from forward modeling. With the 1-D non-gradient-based inversion package we have developed, we further explored the tradeoff between the depth of the discontinuity and the low wave speed gradient above it. In addition, we systematically validated the alignment operation, widely used by previous researchers in the trial-and-error triplication inversion.

Finally, we inverted the 1-D structure below the Tatar Strait of Russia. The derived model shows an uplift interface at 400$\pm$5 km, with a significant wave speed jump of $\sim$ 7%-8%. We propose this interface to be an overlapping of the uplifted 410-km discontinuity and the slab upper interface. Our preferred slab upper interface, from the simultaneous inversion of the interface depth and the wave speed at high frequency, is $\sim$ 50-70 km shallower than the Slab2.0 model and the +2-3% wave speed contours of the regional tomography model (Tao et al. 2018).

ACKNOWLEDGMENTS

Seismic records used in this study came from the NECESSArray and CEArray, and we thank the team members for their deployments. We thank Chunquan Yu for helping with the 2-D simulation and Shawn S. Wei, Mingda Lv, Xiaobo He, Megan Flanagan, Ziyi Xi, Guoliang Li and Zhigang Peng for valuable discussion. We acknowledge the course "English Composition for Geophysical Research" by Li Zhao of Peking University for help in improving this manuscript. We thank the IRIS Data Management Center for the access to waveforms used in the focal depth inversion. We thank the Institute for Cyber-Enabled Research (ICER) at Michigan State University, the Extreme Science and Engineering Discovery Environment (XSEDE supported by NSF grant ACI-1053575), and the High-performance Computing Platform of Peking University for providing the high-performance computing resources. Map-view figure is produced using the GMT software of Wessel & Smith (1998). This research was supported by NSF grant 1802247 and the startup fund of Min Chen at Michigan State University.

REFERENCES

Akaogi, M., Ito, E., & Navrotsky, A., 1989. Olivine-modified spinel-spinel transitions in the system mg2sio4-fe2sio4: Calorimetric measurements, thermochemical calculation, and geophysical application, *Journal of Geophysical Research: Solid Earth*, **94**(B11), 15671–15685.

Benz, H. & Vidale, J., 1993. Sharpness of upper-mantle discontinuities determined from high-frequency reflections, *Nature*, **365**(6442), 147–150.

Bercovici, D. & Karato, S.-i., 2003. Whole-mantle convection and the transition-zone water filter, *Nature*, **425**(6953), 39–44.

Bina, C. R. & Helffrich, G., 1994. Phase transition clapeyron slopes and transition zone seismic discontinuity topography, *Journal of Geophysical Research: Solid Earth*, **99**(B8), 15853–15860.

Brudzinski, M. R. & Chen, W.-P., 2000. Variations in p wave speeds and outboard earthquakes: evidence for a petrologic anomaly in the mantle transition zone, *Journal of Geophysical Research: Solid Earth*, **105**(B9), 21661–21682.

Brudzinski, M. R. & Chen, W.-P., 2003. A petrologic anomaly accompanying outboard earthquakes beneath fiji-tonga: Corresponding evidence from broadband p and s waveforms, *Journal of Geophysical Research: Solid Earth*, **108**(B6).

Chapman, C. H., 1978. A new method for computing synthetic seismograms, *Geophysical Journal International*, **54**(3), 481–518.

Chen, Y. J. & Pei, S., 2010. Tomographic structure of east asia: Ii. stagnant slab above 660 km discontinuity and its geodynamic implications, *Earthquake Science*, **23**(6), 613–626.

Chevrot, S., Vinnik, L., & Montagner, J.-P., 1999. Global-scale analysis of the mantle pds phases, *Journal of Geophysical Research: Solid Earth*, **104**(B9), 20203–20219.

Chu, R., Schmandt, B., & Helmberger, D. V., 2012. Upper mantle p velocity structure beneath the midwestern united states derived from triplicated waveforms, *Geochemistry, Geophysics, Geosystems*, **13**(2).

Collier, J. D. & Helffrich, G. R., 1997. Topography of the "410" and "660" km seismic discontinuities in the izu-bonin subduction zone, *Geophysical research letters*, **24**(12), 1535–1538.

Crotwell, H. P., Owens, T. J., & Ritsema, J., 1999. The taup toolkit: Flexible seismic travel-time and ray-path utilities, *Seismological Research Letters*, **70**(2), 154–160.

Flanagan, M. P. & Shearer, P. M., 1998. Global mapping of topography on transition zone velocity discontinuities by stacking ss precursors, *Journal of Geophysical Research: Solid Earth*, **103**(B2), 2673–2692.

Flanagan, M. P. & Shearer, P. M., 1999. A map of topography on the 410-km discontinuity from pp precursors, *Geophysical research letters*, **26**(5), 549–552.

Fukao, Y., Widiyantoro, S., & Obayashi, M., 2001. Stagnant slabs in the upper and lower mantle transition region, *Reviews of Geophysics*, **39**(3), 291–323.

Gaherty, J. B., Wang, Y., Jordan, T. H., & Weidner, D. J., 1999. Testing plausible upper-mantle compositions using fine-scale models of the 410-km discontinuity, *Geophysical Research Letters*, **26**(11), 1641–1644.

Gao, W., Matzel, E., & Grand, S. P., 2006. Upper mantle seismic structure beneath eastern mexico determined from p and s waveform inversion and its implications, *Journal of Geophysical Research: Solid Earth*, **111**(B8).

Grand, S. P. & Helmberger, D. V., 1984. Upper mantle shear structure of north america, *Geophysical Journal International*, **76**(2), 399–438.

Green Ii, H. & Burnley, P., 1989. A new self-organizing mechanism for deep-focus earthquakes, *Nature*, **341**(6244), 733–737.

Gu, Y. J. & Dziewonski, A. M., 2002. Global variability of transition zone thickness, *Journal of Geophysical Research: Solid Earth*, **107**(B7), ESE–2.

Hayes, G. P., Moore, G. L., Portner, D. E., Hearne, M., Flamme, H., Furtney, M., & Smoczyk, G. M., 2018. Slab2, a comprehensive subduction zone geometry model, *Science*, **362**(6410), 58–61.

Helffrich, G. R. & Wood, B. J., 1996. 410 km discontinuity sharpness and the form of the olivine α-β phase diagram: resolution of apparent seismic contradictions, *Geophysical Journal International*, **126**(2), F7–F12.

Houser, C., Masters, G., Flanagan, M., & Shearer, P., 2008. Determination and analysis of long-wavelength transition zone structure using ss precursors, *Geophysical Journal International*, **174**(1), 178–194.

Huang, J. & Zhao, D., 2006. High-resolution mantle tomography of china and surrounding regions, *Journal of Geophysical Research: Solid Earth*, **111**(B9).

Johnson, L. R., 1967. Array measurements of p velocities in the upper mantle, *Journal of Geophysical Research*, **72**(24), 6309–6325.

Katsura, T., Yamada, H., Nishikawa, O., Song, M., Kubo, A., Shinmei, T., Yokoshi, S., Aizawa, Y., Yoshino, T., Walter, M. J., et al., 2004. Olivine-wadsleyite transition in the system (mg, fe) 2sio4, *Journal of Geophysical Research: Solid Earth*, **109**(B2).

Katsura, T., Yoneda, A., Yamazaki, D., Yoshino, T., & Ito, E., 2010. Adiabatic temperature profile in the mantle, *Physics of the Earth and Planetary Interiors*, **183**(1-2), 212–218.

Kawakatsu, H. & Watada, S., 2007. Seismic evidence for deep-water transportation in the mantle, *Science*, **316**(5830), 1468–1471.

Kennett, B. & Engdahl, E., 1991. Traveltimes for global earthquake location and phase identification, *Geophysical Journal International*, **105**(2), 429–465.

King, S. D., Frost, D. J., & Rubie, D. C., 2015. Why cold slabs stagnate in the transition zone, *Geology*, **43**(3), 231–234.

Kirby, S. H., Durham, W. B., & Stern, L. A., 1991. Mantle phase changes and deep-earthquake faulting in subducting lithosphere, *Science*, **252**(5003), 216–225.

Koper, K. D., Wysession, M. E., & Wiens, D. A., 1999. Multimodal function optimization with a niching genetic algorithm: A seismological example, *Bulletin of the Seismological Society of America*, **89**(4), 978–988.

Lawrence, J. F. & Shearer, P. M., 2008. Imaging mantle transition zone thickness with sds-ss finite-frequency sensitivity kernels, *Geophysical Journal International*, **174**(1), 143–158.

LeFevre, L. V. & Helmberger, D. V., 1989. Upper mantle p velocity structure of the canadian shield, *Journal of Geophysical Research: Solid Earth*, **94**(B12), 17749–17765.

Li, D., Helmberger, D., Clayton, R. W., & Sun, D., 2014. Global synthetic seismograms using a 2-d finite-difference method, *Geophysical Journal International*, **197**(2), 1166–1183.

Li, J., Wang, S., C. C., & Ning, J., 2016. A computational scheme for quantitatively removing the effects of lateral velocity variation on 1-d triplicated wave velocity inversion, *Acta Scientiarum Naturalium Universitatis Pekinensis*, **52**(3), 420–426.

Li, L., Chen, Y.-W., Zheng, Y., Hu, H., & Wu, J., 2019. Seismic evidence for plume-slab interaction by high-resolution imaging of the 410-km discontinuity under tonga, *Geophysical Research Letters*, **46**(23), 13687–13694.

Li, S.-H., Wang, Y.-B., Liang, Z.-B., He, S.-L., & Wen-Hao, Z., 2012. Crustal structure in southeastern gansu from regional seismic waveform inversion, *Chinese Journal of Geophysics*, **55**(2), 206–218.

Melbourne, T. & Helmberger, D., 1998. Fine structure of the 410-km discontinuity, *Journal of Geophysical Research: Solid Earth*, **103**(B5), 10091–10102.

Neele, F., 1996. Sharp 400-km discontinuity from short-period p reflections, *Geophysical research letters*, **23**(5), 419–422.

Niu, F., Levander, A., Ham, S., & Obayashi, M., 2005. Mapping the subducting pacific slab beneath southwest japan with hi-net receiver functions, *Earth and Planetary Science Letters*, **239**(1-2), 9–17.

Revenaugh, J. & Sipkin, S., 1994. Seismic evidence for silicate melt atop the 410-km mantle discontinuity, *Nature*, **369**(6480), 474–476.

Ringwood, A. E., 1968. Phase transformations in the mantle, *Earth and Planetary Science Letters*, **5**, 401–412.

Ringwood, A. E., 1975. Composition and petrology of the earth's mantle, *MacGraw-Hill*, **618**.

Ritsema, J., Cupillard, P., Tauzin, B., Xu, W., Stixrude, L., & Lithgow-Bertelloni, C., 2009a. Joint mineral physics and seismic wave traveltime analysis of upper mantle temperature, *Geology*, **37**(4), 363–366.

Ritsema, J., Xu, W., Stixrude, L., & Lithgow-Bertelloni, C., 2009b. Estimates of the transition zone temperature in a mechanically mixed upper mantle, *Earth and Planetary Science Letters*, **277**(1-2), 244–252.

Schmandt, B., Dueker, K., Hansen, S., Jasbinsek, J. J., & Zhang, Z., 2011. A sporadic low-velocity layer atop the western us mantle transition zone and short-wavelength variations in transition zone discontinuities, *Geochemistry, Geophysics, Geosystems*, **12**(8).

Schmerr, N. & Garnero, E. J., 2007. Upper mantle discontinuity topography from thermal and chemical heterogeneity, *Science*, **318**(5850), 623–626.

Shearer, P. M., 2000. Upper mantle seismic discontinuities, *GEOPHYSICAL MONOGRAPH-AMERICAN GEOPHYSICAL UNION*, **117**, 115–132.

Song, T.-R. A., Helmberger, D. V., & Grand, S. P., 2004. Low-velocity zone atop the 410-km seismic discontinuity in the northwestern united states, *Nature*, **427**(6974), 530–533.

Tajima, F. & Grand, S. P., 1995. Evidence of high velocity anomalies in the transition zone associated with southern kurile subduction zone, *Geophysical research letters*, **22**(23), 3139–3142.

Tao, K., Grand, S. P., & Niu, F., 2017. Full-waveform inversion of triplicated data using a normalized-correlation-coefficient-based misfit function, *Geophysical Journal International*, **210**(3), 1517–1524.

Tao, K., Grand, S. P., & Niu, F., 2018. Seismic structure of the upper mantle beneath eastern asia from full waveform seismic tomography, *Geochemistry, Geophysics, Geosystems*, **19**(8), 2732–2763.

Thirot, J.-L., Montagner, J.-P., & Vinnik, L., 1998. Upper-mantle seismic discontinuities in a subduction zone (japan) investigated from p to s converted waves, *Physics of the earth and planetary interiors*, **108**(1), 61–80.

Tian, D., Lv, M., Wei, S. S., Dorfman, S. M., & Shearer, P. M., 2020. Global variations of earth's 520-and 560-km discontinuities, *Earth and Planetary Science Letters*, **552**, 116600.

Tibi, R. & Wiens, D. A., 2005. Detailed structure and sharpness of upper mantle discontinuities in the tonga subduction zone from regional broadband arrays, *Journal of Geophysical Research: Solid Earth*, **110**(B6).

Van der Meijde, M., Marone, F., Giardini, D., & Van der Lee, S., 2003. Seismic evidence for water deep in earth's upper mantle, *Science*, **300**(5625), 1556–1558.

Vidale, J. E., Ding, X.-Y., & Grand, S. P., 1995. The 410-km-depth discontinuity: A sharpness estimate from near-critical reflections, *Geophysical research letters*, **22**(19), 2557–2560.

Vinnik, L., 1977. Detection of waves converted from p to sv in the mantle, *Physics of the Earth and planetary interiors*, **15**(1), 39–45.

Wang, B. & Niu, F., 2010. A broad 660 km discontinuity beneath northeast china revealed by dense regional seismic networks in china, *Journal of Geophysical Research: Solid Earth*, **115**(B6).

Wang, R., 1999. A simple orthonormalization method for stable and efficient computation of green's functions, *Bulletin of the Seismological Society of America*, **89**(3), 733–741.

Wang, T. & Chen, L., 2009. Distinct velocity variations around the base of the upper mantle beneath northeast asia, *Physics of the Earth and Planetary Interiors*, **172**(3-4), 241–256.

Wang, T., Revenaugh, J., & Song, X., 2014. Two-dimensional/three-dimensional waveform modeling of subducting slab and transition zone beneath northeast asia, *Journal of Geophysical Research: Solid Earth*, **119**(6), 4766–4786.

Wang, X., Li, J., & Chen, Q.-F., 2017. Topography of the 410 km and 660 km discontinuities beneath the japan sea and adjacent regions by analysis of multiple-scs waves, *Journal of Geophysical Research: Solid Earth*, **122**(2), 1264–1283.

Wang, Y., Wen, L., & Weidner, D., 2009. Array triplication data constraining seismic structure and composition in the mantle, *Surveys in geophysics*, **30**(4-5), 355–376.

Wei, S. S. & Shearer, P. M., 2017. A sporadic low-velocity layer atop the 410 km discontinuity beneath the pacific ocean, *Journal of Geophysical Research: Solid Earth*, **122**(7), 5144–5159.

Wei, S. S., Shearer, P. M., Lithgow-Bertelloni, C., Stixrude, L., & Tian, D., 2020. Oceanic plateau of the hawaiian mantle plume head subducted to the uppermost lower mantle, *Science*, **370**(6519), 983–987.

Wessel, P. & Smith, W. H., 1998. New, improved version of generic mapping tools released, *Eos, Transactions American Geophysical Union*, **79**(47), 579–579.

Xu, W., Lithgow-Bertelloni, C., Stixrude, L., & Ritsema, J., 2008. The effect of bulk composition and temperature on mantle seismic structure, *Earth and Planetary Science Letters*, **275**(1-2), 70–79.

Ye, L., Li, J., Tseng, T.-L., & Yao, Z., 2011. A stagnant slab in a water-bearing mantle transition zone beneath northeast china: implications from regional sh waveform modelling, *Geophysical Journal International*, **186**(2), 706–710.

Zhang, M., Sun, D., Wang, Y., & Wu, Z., 2019. Fine structure of the 660-km discontinuity beneath southeastern china, *Geophysical Research Letters*, **46**(13), 7304–7314.

Zhang, R., Wu, Q., Li, Y., & Romanowicz, B., 2012. Lateral variations in sh velocity structure of the transition zone beneath korea and adjacent regions, *Journal of Geophysical Research: Solid Earth*, **117**(B9).

Zheng, X.-F., Yao, Z.-X., Liang, J.-H., & Zheng, J., 2010. The role played and opportunities provided by igp dmc of china national seismic network in wenchuan earthquake disaster relief and researches, *Bulletin of the Seismological Society of America*, **100**(5B), 2866–2872.

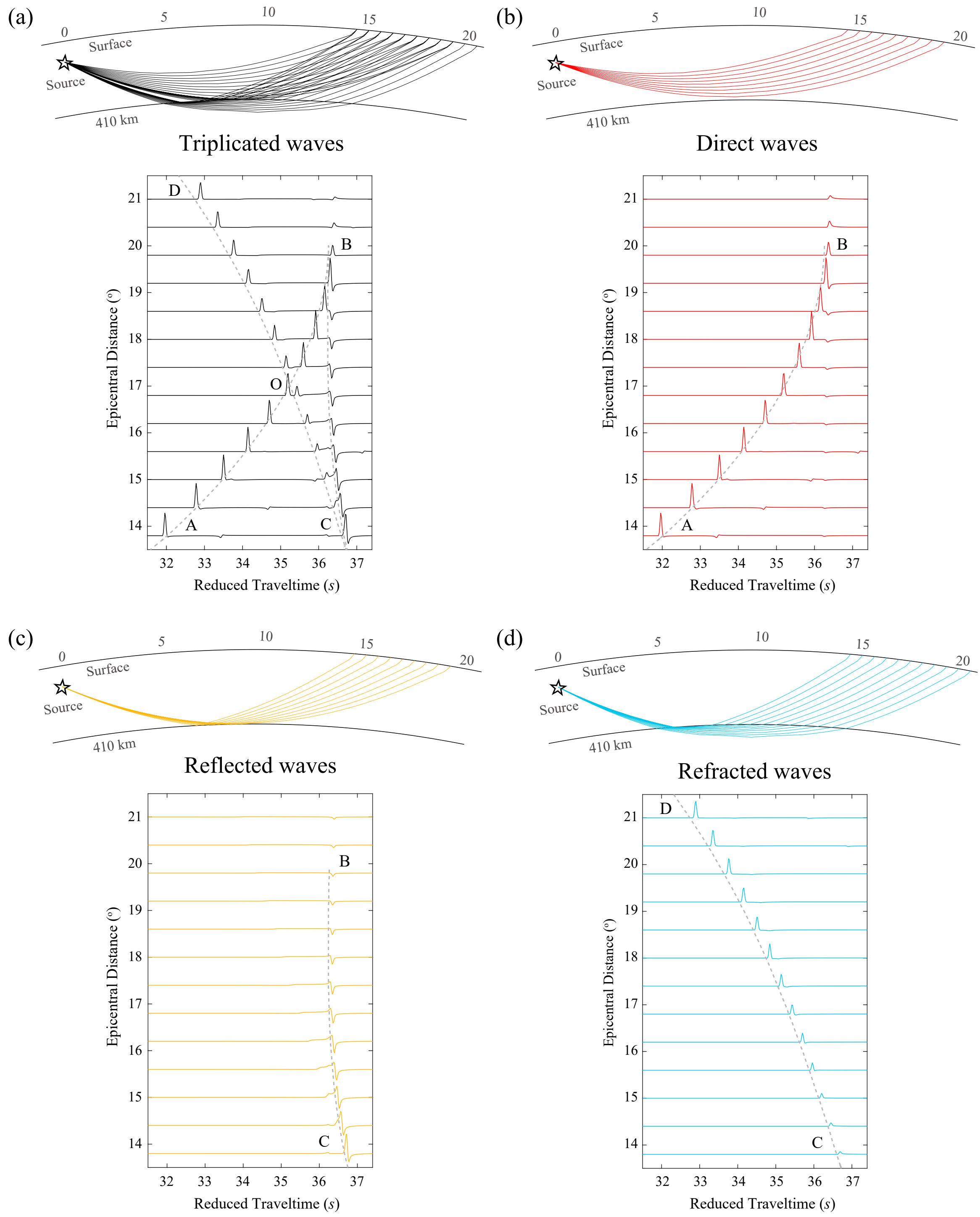

Figure 1. Ray paths and corresponding waveforms for triplication. (a) Ray paths and waveforms for all the triplicated P waves. In the upper panel, the black star is the earthquake source at 114km, and black lines show all the triplicated P ray paths. In the lower panel, the black waveforms are synthetics calculated by WKBJ (Chapman 1978) for the IASP91 model (Kennett & Engdahl 1991), and the dashed grey lines are the corresponding travel time curves calculated by Taup (Crotwell et al. 1999). AB, BC, and CD branches represent the direct waves, reflected waves and refracted waves, respectively. The O point shows the cross over point of the AB and BC branch. A reducing slowness of 11.5 s/^{o} is used for the time plot. (b) Ray paths and waveforms for the direct waves AB with red color. (c) Ray paths and waveforms for the reflected waves BC with yellow color. (d) Ray paths and waveforms for the refracted waves CD with blue color.

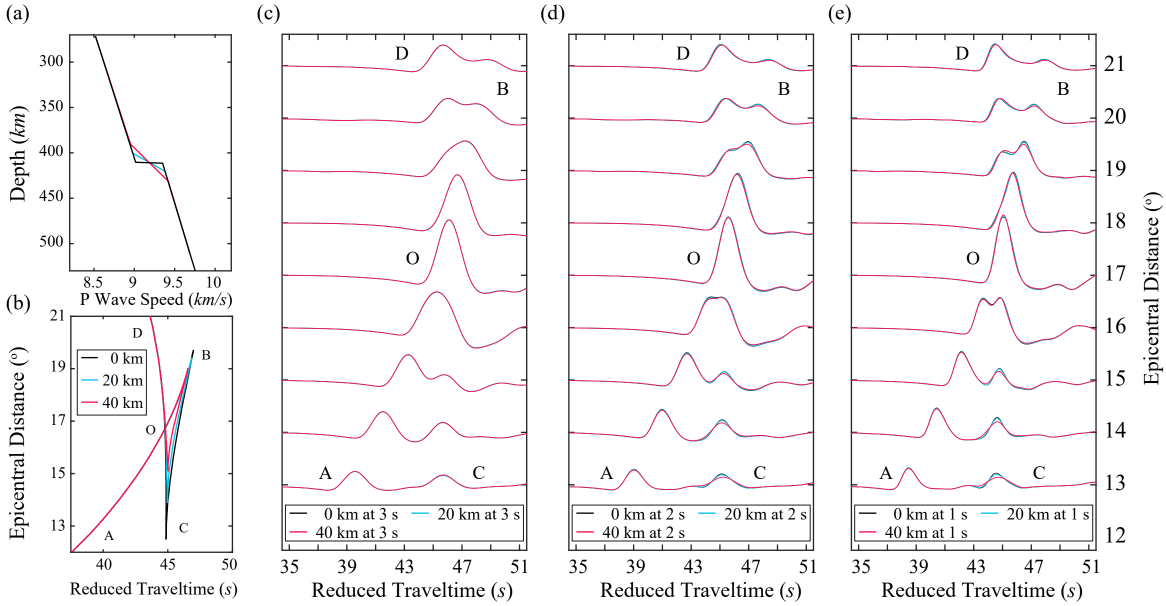

Figure 2. Modeling tests for the effect of the sharpness of the interface on the triplication. (a) Models used in the synthetic test. The black line is the IAPS91 model (Kennett & Engdahl 1991), while the blue and red lines are models in which the 410-km discontinuity is replaced by a gradual transition with thicknesses of 20 km and 40 km, respectively. (b) Corresponding travel time curves plotted in the same color as the models in (a). (c) Synthetic waveforms corresponding to models of the same colors in (a). Although there are significant differences in the travel time curves as shown in (b), the waveforms are almost the same with a period of 3 s. (d) Synthetic waveforms comparison with a period of 2 s. Black and red waveforms correspond to models of the same colors in (a). (e) Synthetic waveforms comparison with a period of 1 s. Black and red waveforms correspond to models of the same colors in (a).

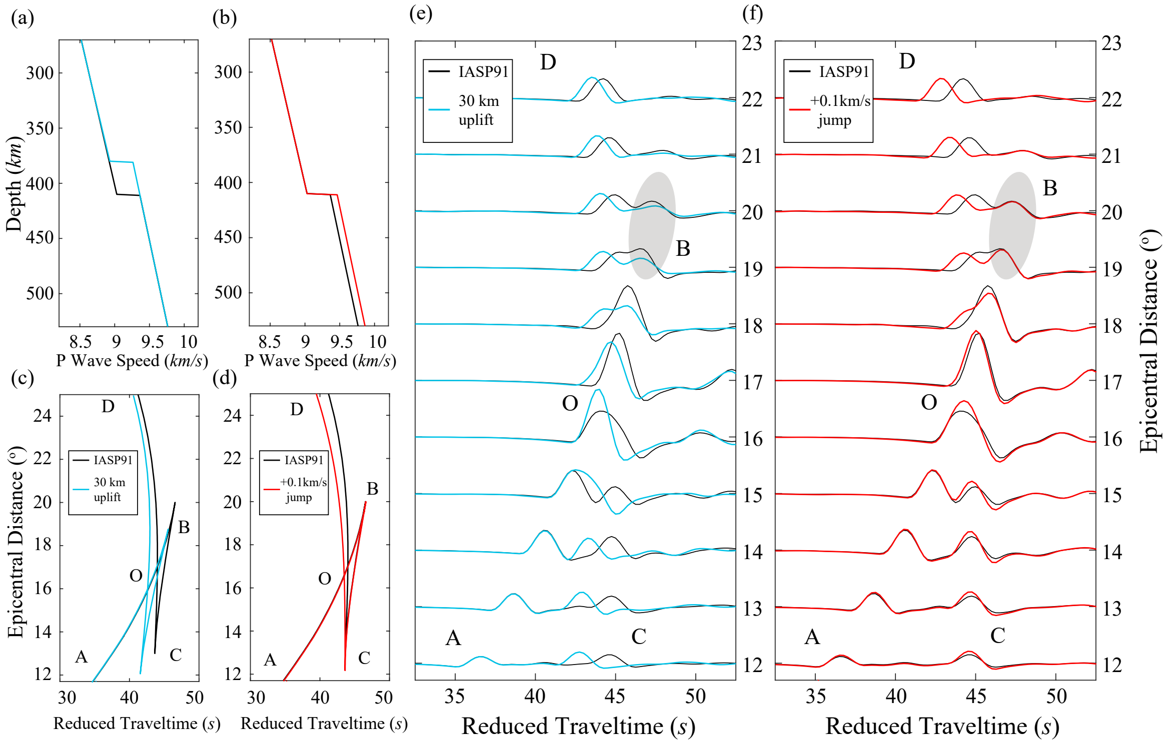

Figure 3. Modeling tests for the influence of topography and wave speed jump. (a) Black line shows the IASP91 model (Kennett & Engdahl 1991), whereas the blue line is the model with a 30-km uplift for the 410-km discontinuity. (b) Black line shows the IASP91 model, whereas the red line is the model with a +0.1 km/s wave speed jump across the 410-km discontinuity. (c) Travel time curves for the IASP91 model (black line) and the model with a 30-km uplift (blue line). AB, BC and CD indicate direct, reflected and refracted waves, respectively. O denotes the crossover point of AB and CD branch. (d) Travel time curves for the IASP91 model (black line) and the model with a +0.1 km/s wave speed jump across the 410-km discontinuity (red line). (e) Waveform comparison between the model with a 30-km uplift (blue) and the IASP91 model (black). A reducing slowness of 11 s/^{o} is used for the time plot. (f) Waveform comparison between the model with a +0.1km/s wave speed jump across the 410-km discontinuity (red) and the IASP91 model (black).

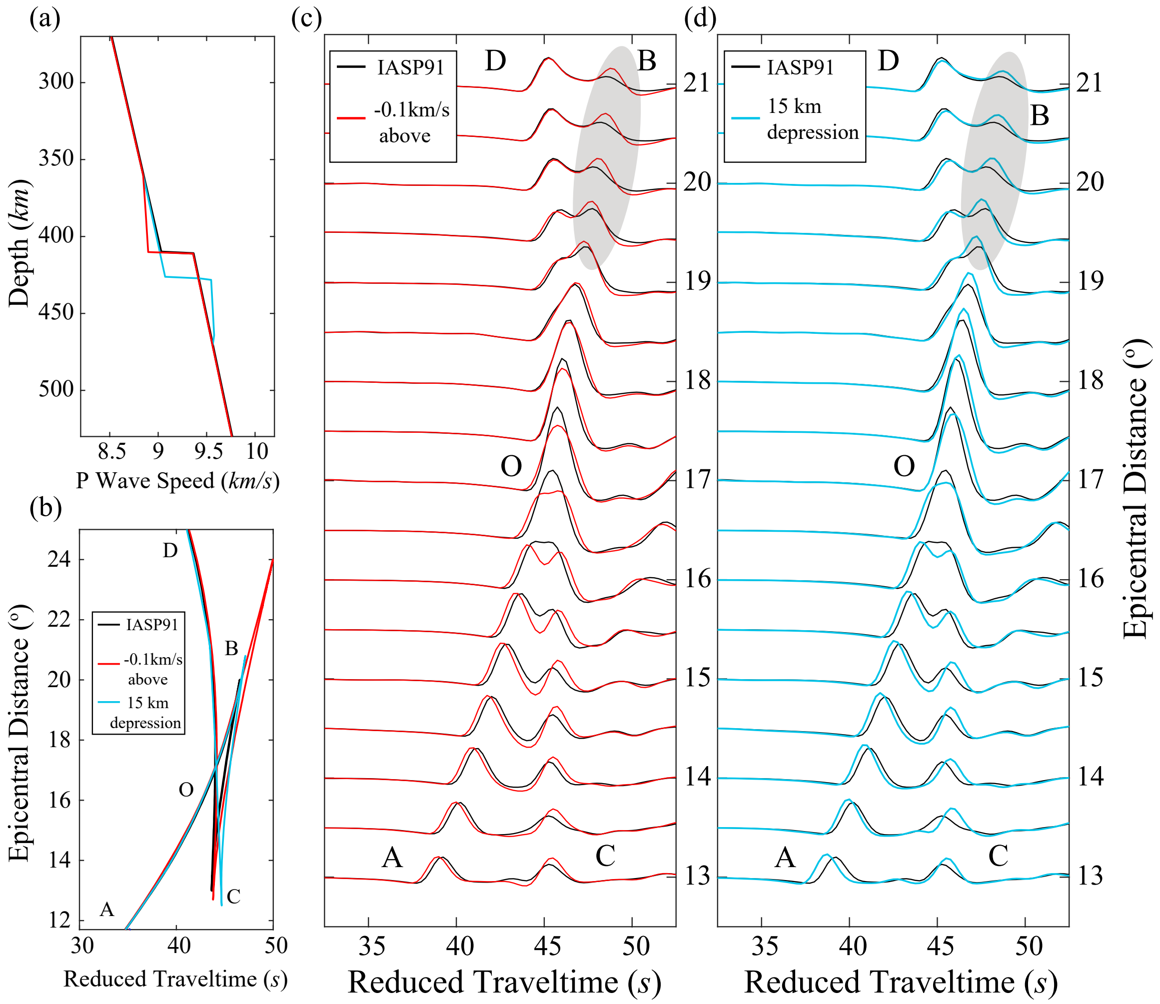

Figure 4. Modeling tests for the tradeoff between the low wave speed zone above the interface and a depressed topography. (a) Black line shows the IASP91 model (Kennett & Engdahl 1991), the red line shows the model with a low wave speed zone above the discontinuity, and the blue line is the model with a 15-km depression for the discontinuity. (b) Travel time curves for the IASP91 model (black line) and the model with a -0.1km/s low wave speed zone above the discontinuity (red line). AB, BC and CD indicate direct, reflected and refracted waves, respectively. O denotes the crossover point of AB and CD branch. (c) Waveform comparison between the reference IASP91 model (black) and the model with a low wave speed zone above the discontinuity (red). The most obvious difference is the increased amplitude near the cusp B. (d) Waveform comparison between the reference IASP91 model (black) and the model with a 15-km depression for the discontinuity (blue). Amplitude near the cusp B also increases for this model.

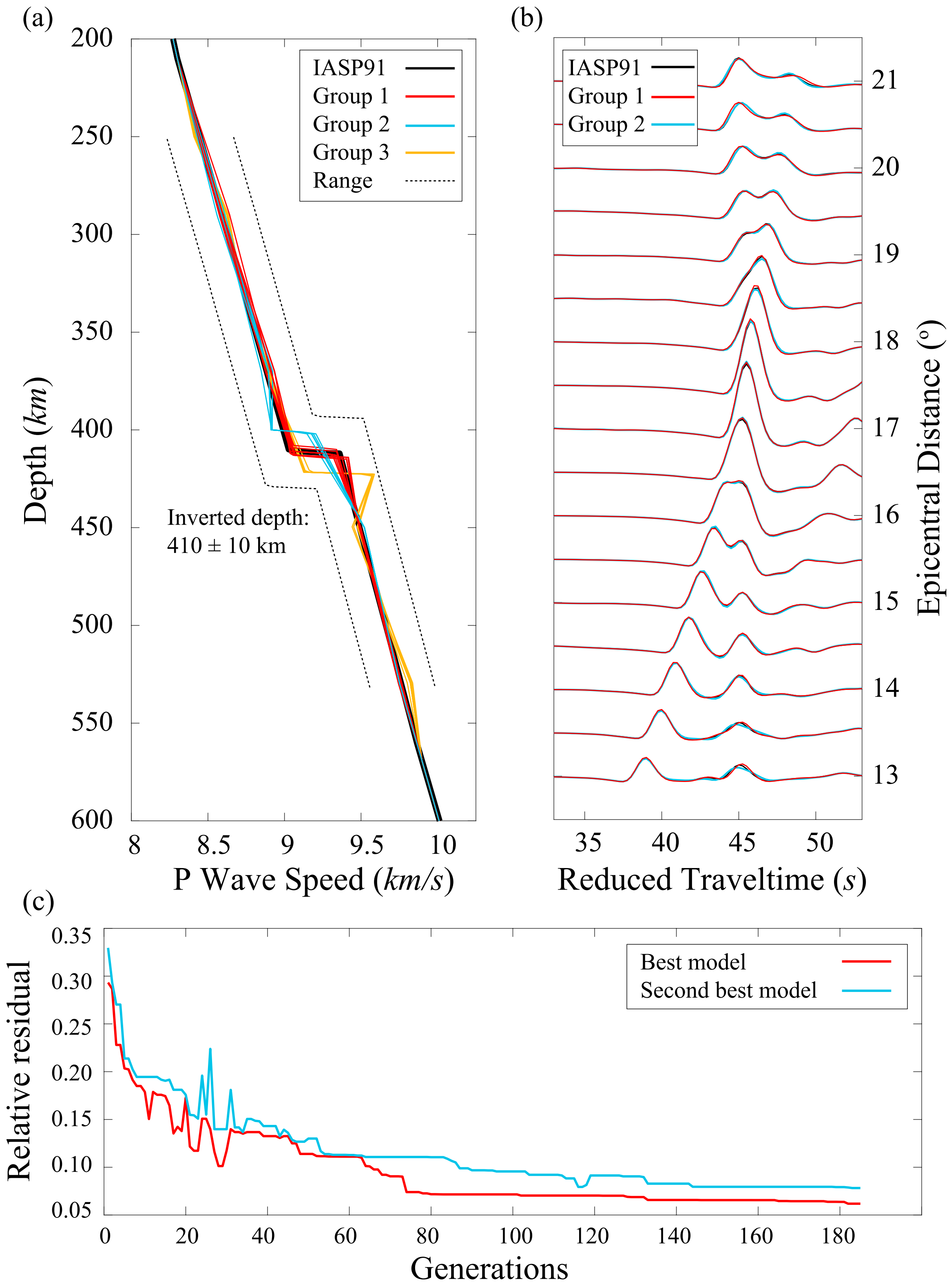

Figure 5. Synthetic tests for Niche Genetic Algorithm. (a) Inverted models. Black solid line is the IASP91 model (Kennett & Engdahl 1991). Red, blue and yellow lines show different groups of the acceptable models. The dotted black lines represent the model searching range. (b) Waveform fitting. Black waveforms are synthetics for the IASP91 model, red waveforms are synthetics for one of the models from model group one, and blue waveforms are synthetics for one of the models from model group two. (c) Residual between data and synthetics with respect to generations. The red and blue lines are the residual for the best and second best models, respectively.

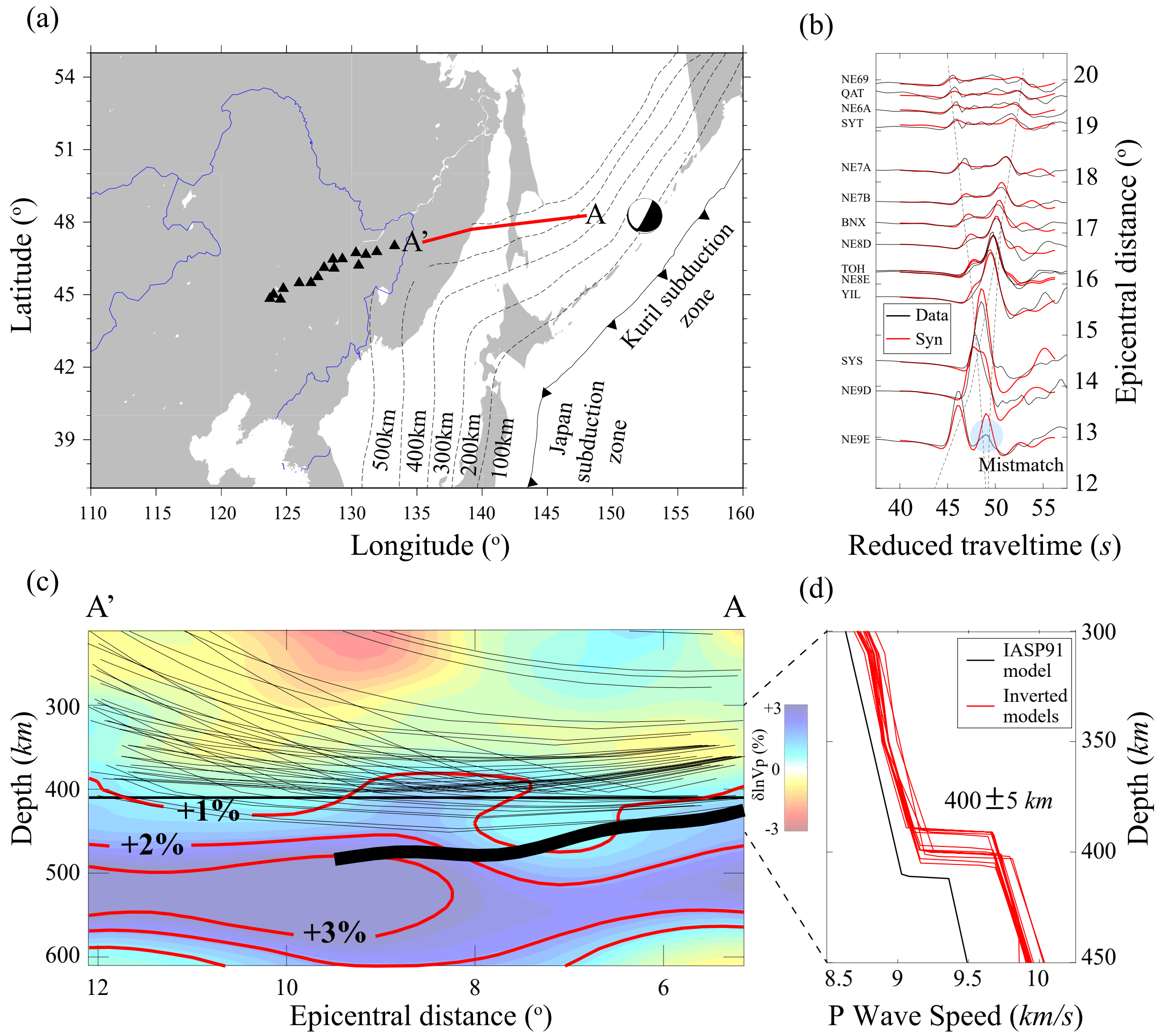

Figure 6. Research region and inversion results. (a) Research region and the distribution of stations and event. The black beach ball and black triangles represent the event and stations respectively. Red line shows the location of the cross-section AA' in (c). Black dashed lines are the depth contours of the subduction zone, with numbers showing the corresponding depths. (b) Displacement waveform comparison between data and synthetics in the vertical component for P wave. A reducing slowness of 11 s/o is used for the time plot. For each trace, the station name is given on the left. The red waveform is the synthetic waveform for the best model, and its duration represents the length of the misfit window used. The black waveform is recorded waveform after alignment with the synthetic one by cross-correlation. And dashed grey lines show the corresponding travel-time curves calculated by Taup Toolkit (Crotwell et al. 1999). The blue circle marks the mismatched reflected phase for station 'NE9E'. (c) Cross-section AA' as shown in (a). The background is from the FWEA18 tomography model (Tao et al. 2018), and the red lines are its wave speed contour. The bold black line is the location of the slab upper interface from Slab2.0 model (Hayes et al. 2018). The grey lines are the ray paths. (d) P wave speed inversion results. The red lines show the inverted acceptable models, whereas the black line indicates the IASP91 model (Kennett & Engdahl 1991). The depth range from 300 km to 450 km is the most reliable region where the ray paths (grey lines) are dense enough as shown in (c).

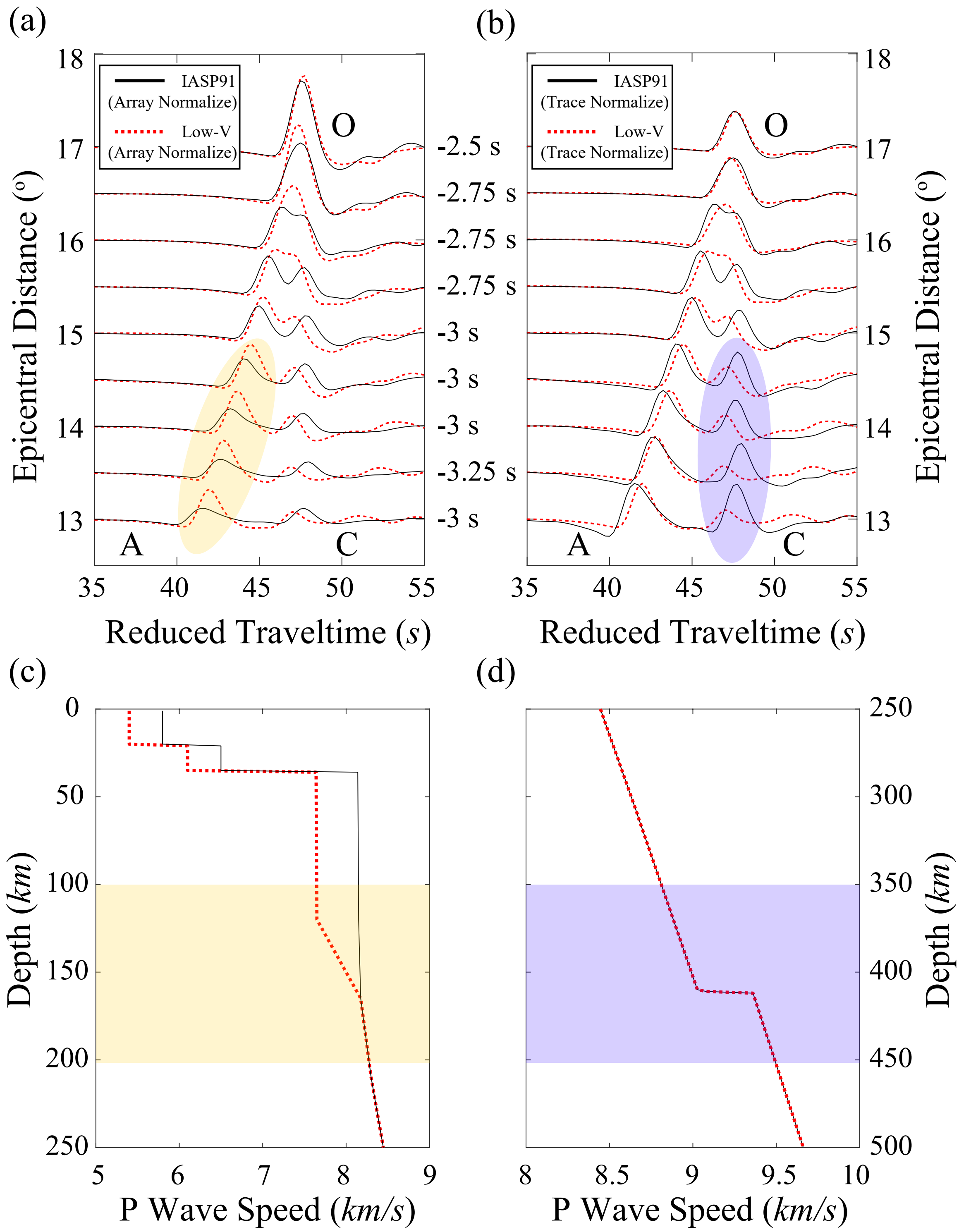

Figure 7. Comparison between trace normalization and array normalization. (a) Array-normalized waveforms. Solid black waveforms are synthetics for the IASP91 model (Kennett & Engdahl 1991) and dotted red waveforms are for the red model in (c). Yellow region shows where the amplitudes are different. Number near the end of each trace denotes the time delay (∼ 3 s) for each station. (b) Trace-normalized waveforms. Blue dashed oval shows the where the waveforms are different. (c) Shallow portion of the model. The solid black line is the IASP91 model, and the dotted red line is the designed model with a -0.4km/s zone in the top 160 km. Yellow box shows where the wave speed gradient changes. (d) Deep portion of the model. Blue box roughly shows where we tend to modify when applying the trace normalization.

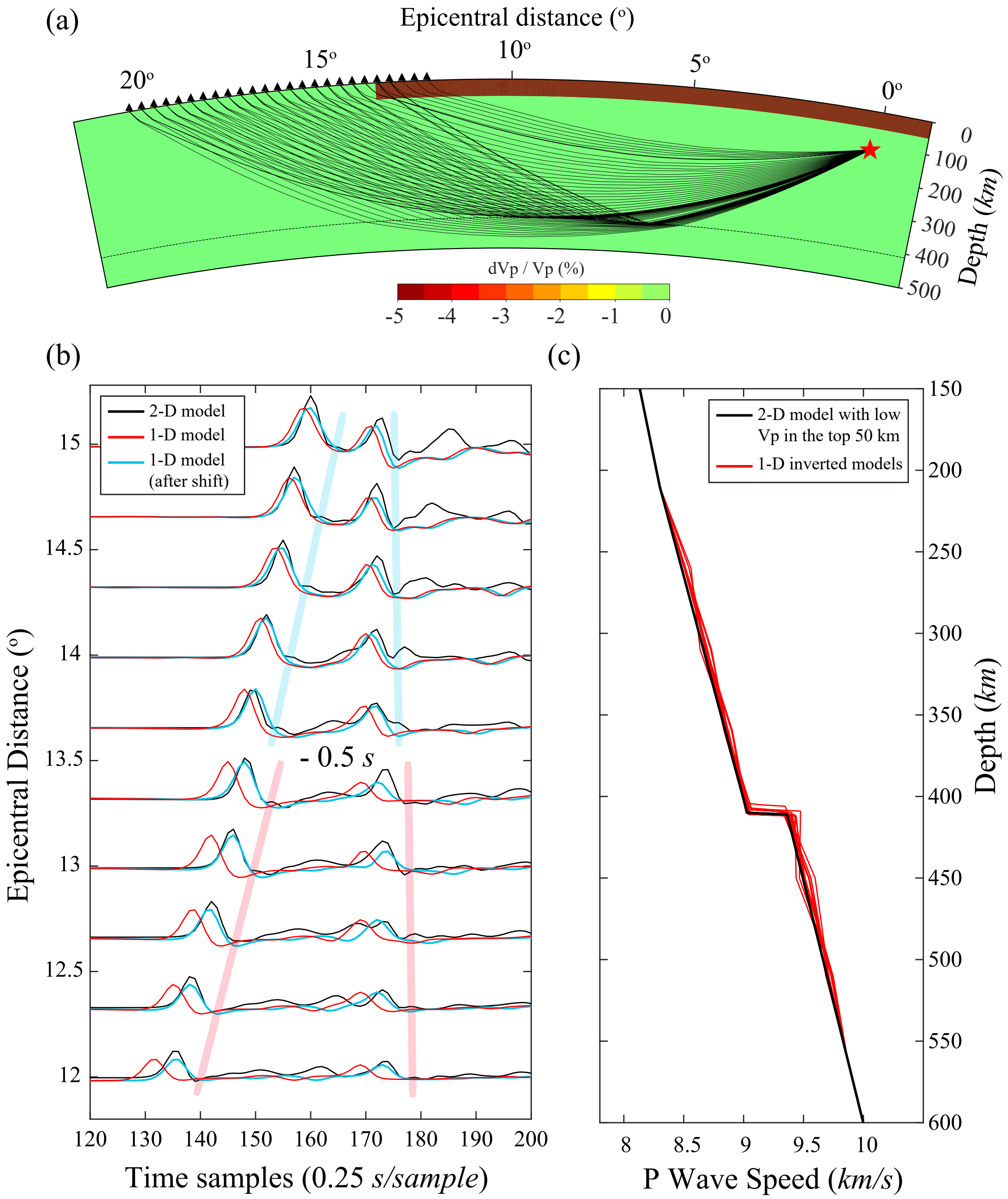

Figure 8. Synthetic tests for inaccurate 2-D structure at shallow depth. (a) The 2-D model used in the synthetic test. The background is the IASP91 model (Kennett & Engdahl 1991), and the wave speed in the red region shows a -0.3km/s anomaly. The red star is the earthquake, and the black triangles are the stations. Black lines are ray paths calculated by Taup Toolkit (Crotwell et al. 1999) for the 1-D IASP91 model. The maximum epicentral distance influenced by the low wave speed anomaly is around 13.5°. (b) Waveform comparison. The black waveforms are the synthetics for the 2-D groud truth model in (a) using a 2-D finite difference algorithm (Li et al. 2014) and the red waveforms are the synthetics for one of the models in (c). The blue waveforms are the red synthetics after aligning with the black waveforms by cross-correlation. The bold red and blue lines roughly show the travel time curves for the delayed and normal traces, respectively. (c) Inverted 1-D models. The solid black line is the deeper part of the ground truth model, which is the same as the IASP91 model in this depth range, and the solid red lines are the models from the best model group.